nanomaterials

MDPI

Article

Computational Analysis of the Morphological Aspects of Triadic Hybridized Magnetic Nanoparticles Suspended in Liquid Streamed in Coaxially Swirled Disks

Zubair Akbar Qureshi [1,*], Sardar Bilal [2,*], Imtiaz Ali Shah [2], Ali Akgül [3], Rabab Jarrar [4], Hussein Shanak [4] and Jihad Asad [4]

[1] Department of Mathematics, Multan Campus, AIR University, Multan 49501, Pakistan
[2] Department of Mathematics, AIR University, Islamabad 44000, Pakistan; imtiazsha91@gmail.com
[3] Department of Mathematics, Art and Science Faculty, Siirt University, Siirt 56100, Turkey; aliakgul00727@gmail.com
[4] Department of Physics, Faculty of Applied Sciences, Palestine Technical University-Kadoorie, Tulkarm 305, West Bank, Palestine; r.jarrar@ptuk.edu.ps (R.J.); h.shanak@ptuk.edu.ps (H.S.); j.asad@ptuk.edu.ps (J.A.)
* Correspondence: zubair@aumc.edu.pk (Z.A.Q.); sardarbilal@mail.au.edu.pk (S.B.)

Abstract: Currently, pagination clearly explains the increase in the thermophysical attributes of viscous hybrid nanofluid flow by varying morphological aspects of inducted triadic magnetic nanoparticles between two coaxially rotating disks. Copper metallic nanoparticles are inserted with three different types of metallic oxide nanoparticles: Al_2O_3, Ti_2O, and Fe_3O_4. Single-phase simulation has been designed for the triadic hybrid nanofluids flow. The achieved expressions are transmuted by the obliging transformation technique because of dimensionless ordinary differential equations (ODEs). Runge–Kutta in collaboration with shooting procedure are implemented to achieve the solution of ODEs. The consequences of pertinent variables on associated distributions and related quantities of physical interest are elaborated in detail. It is inferred from the analysis that Cu-Al_2O_3 metallic type hybrid nanofluids flow shows significant results as compared with the other hybrid nanoparticles. The injection phenomenon on hybrid nanofluids gives remarkable results regarding shear stress and heat flux with the induction of hybridized metallic nanoparticles. Shape and size factors have also been applied to physical quantities. The morphology of any hybrid nanoparticles is directly proportional to the thermal conductance of nanofluids. Peclet number has a significant effect on the temperature profile.

Keywords: triadic hybridize nanofluid model; heat and mass flux; MHD; morphology effect; computational analysis (shooting technique)

Citation: Qureshi, Z.A.; Bilal, S.; Shah, I.A.; Akgül, A.; Jarrar, R.; Shanak, H.; Asad, J. Computational Analysis of the Morphological Aspects of Triadic Hybridized Magnetic Nanoparticles Suspended in Liquid Streamed in Coaxially Swirled Disks. *Nanomaterials* **2022**, *12*, 671. https://doi.org/10.3390/nano12040671

Academic Editors: M.M. Bhatti, Kambiz Vafai and Sara I. Abdelsalam

Received: 1 October 2021
Accepted: 27 January 2022
Published: 17 February 2022

1. Introduction

Copper is a transitional metal and possesses the ability to accept and donate electrons along with the characteristic to carry out oxidization and reduction. Because of this tendency, it is used as an essential micronutrient for functionality of living organisms and development of enzymes involved in metabolic processes [1,2]. Moreover, copper contributes to the cure of heart disease, diabetes, and obesity by the formation of drugs [3–7]. In recent years, advancement in nanotechnology has generated intent toward findings of innovative procedures for the production of copper particles on the nano scale (1–100 nm). Especially, metallic nanoparticles including copper particles are widely used in medicinal instruments, investigative imaging, drug supply procedure, therapeutics, and cancers cells. In spite of excellent utilizations of copper nanoparticles, some serious dangers of such nanoparticles are continuously elevated as a result of tissue damaging [8–10]. For this purpose, hybridization of copper with non-metallic oxides is performed, which makes a new class of

working liquids. Extensive experimental research on hybrid nanocomposites can be found, e.g., Turcu et al. [11] and Jana et al. [12]. Furthermore, Devi and Devi [13,14] examined the consequence of hybridized nanoliquid over stretchable configuration and concluded on enhancement in the thermal rate with inclusion of hybridized nanoparticles in base fluid. Farooq et al. [15] analyzed the flow of bio convective cross nanofluid with motile microorganisms in the attendance of radiative energy and melting phenomenon. Anitha et al. [16] evaluated the performance of a double heat exchanger by considering two different hybrid nanofluids composed of water and ethylene as base liquids and TiO_2-γ-AlOOH nanoparticles. Ebrahimi et al. [17] showed modelling of laminarly convective heat transfer of nanoliquid in an enclosure by implementing the finite element approach.

Rotating flows is one of the basic frameworks in the dynamics of liquids. The pioneering work in this direction was performed by Karman [18], who developed the formulation of such a problem by forming the Navier–Stokes equation in curvilinear coordinates. Following the work presented by Karman, extensive works on rotational flows have been performed, such as Griffiths [19], who executed the flow mechanism of non-Newtonian liquid over a spinning disk. Some valuable and old literature related to rotational flow problems is encapsulated in [20–24]. Waini et al. [25] examined the influence of hybrid copper and aluminum oxide nanoparticles in heat transfer elevation of water on a rotating disk. Turkyilmazoglu [26] inspected the single-phase flow of nanofluid over a rotated disk by determining Brownian diffusion aspects. Turkyilmazoglu [27] analyzed 3D laminar flow of electrically conducting viscous liquid flowing over a rotating disk. Some recent acquisitions on rotatory flow problems are divulged in [28–31].

Synthetic characteristics of hybrid nanoparticles along with superior fluidity and stability properties and practical utilization of these composite particles have been raised in different technological applications such as electronic cooling devices, thermal control of vehicles, welding, power systems, lubrication, hydroelectric manufacturing, production of paper and biomedicine, nuclear production, manufacture of spacecraft devices, and many other areas [32–34]. Xu et al. [35] explained the unsteady mixed convective flow of a hybrid nanoliquid between spinning disks. The influence of Hall current and magnetic field on hybrid nanoliquid flow between coaxially rotated disks was encapsulated by Nilankush et al. [36]. Dinarvand et al. [37] computationally scrutinized the flow behavior of a hybrid nanofluid over a porous rotating disk with induction of metallic-oxide (ZuO-Au). Khan et al. [38] probed impression of the Hall effect on a hybrid nanoliquid flowing on a spherical surface. Izadi et al. [39] delineated convective heat transfer in a water hybrid nanofluid with induction of multi-wall carbon nanotubes inside an enclosure. Arani et al. [40] depicted the heat and flow characteristics of a laminar water-based nanoliquid in a novel design of a double-layered microchannel heat sink. Safaei et al. [41] presented work on the thermal aspects of functionalized multi-walled carbon nanotubes in nanoliquid flow over a flat plate by performing numerical simulations. Goshayeshi et al. [42] determined the influence of the shape and size of nanoparticles in elevation in the heat transfer rate of a pulsating heat pipe under the influence of magnetic field. An overview about work conducted by a researcher regarding a hybrid nanoliquid over rotating disks is accumulated in [43,44].

Combined evaluation of heat and mass transfer phenomenon has superb applications in chemical and food processing, hydrometallurgy, ceramics manufacturing, polymerization, and so forth. Vajravelu et al. [45] analyzed magnetically effected 3D squeezed flow of the nanoliquid between rotating discs with velocity slip. Das et al. [46] presented mathematical modelling of magnetically influenced squeezed nanoliquid flow between coaxially rotating disks. Heat and mass transfer aspects in MHD squeezed flow with dispersion of nanoparticles by providing slip effects on surface of disk were deliberated by Din et al. [47]. Qayyum et al. [48] studied heat and mass change in nanofluid thermal flux across a spinning disk with a uniform thin layer. Aziz et al. [49] adumbrated heat and mass transport in dissipated and magnetized flow of viscous fluid over a spinning disk. Reddy et al. [50] presented an analysis on enhancement in convective heat and mass

transfer with the addition of metallic hybridized metallic nanoparticles in fluid flow over a rotating disk.

MHD is the study of the fluid flow mechanism under the influence of magnetic field. Magnetized fluid possesses significant applications in different fields, especially in biomedical science like laser beam scanning, drug delivery targeting, manipulation of nanoparticles, MHD base micropump, magnetic rays imaging, and many others. Muhammad et al. [51] probed the flow of viscoelastic liquid under the impact of magnetic field. Uddin et al. [52] discussed the impact of magnetization on nano viscous liquid over a rotating permeable disk. The effects of magnetic field on viscously dissipated hybrid nanofluids by performing numerical simulations were reported by Imran et al. [53]. Khan et al. [54] evaluated the magnetic field effect on flow features of viscous liquid between coaxially rotated disks. Some recent literature surveys regarding the influence of magnetic field on fluid flow problem in multiple computational domains and under the consideration of various physical variables are accumulated like Krishna et al. [55,56] discussed the consequence of magnetic field along with hall and ion slip on second grade rotating fluid on a semi-infinite vertically moving surface. 3D convective heat transfer in micro concentrated annulus generated by non-uniform heat flux at wall in water base nanofluid with induction of Al_2O_3 nanoparticles was determined by Davood et al. [57]. Some recent developments on MHD fluid in different computation domains are gathered in [58–67].

Examination of fluid flow phenomenon in porous orthogonal disks has numerous dedicated utilizations in many advanced technologies, such as lubricants bearing technology, mass and heat exchanger, viscometers, crystal growth, biomechanics, oceanography, and computer storage system. In this geometry, the foremost physical aspect is the injection/suction along with consideration of hybrid nanofluids, which makes this problem more remarkable in view of practical essence. So, the main objective here is to investigate the enhancement in the thermophysical characteristics of water by inserting triadic hybridized nanoparticles in flow between two orthogonally moving permeable disks. After reviewing the aforementioned literature, consideration of triadic nano particles inside fluid domains is not scrutinized yet. Therefore, the prime concern of this pagination is to inspect the behavior of flow concerning profiles like shear stress, velocity, temperature, and mass profile for injection/suction cases with the addition of triadic particles. A solution to the problem at hand is heeded by implementing the shooting technique and a comparison of computed data with published literature is revealed.

2. Problem Formulation

Here, we assume unsteady, laminarly, and 3D viscous liquid over rotating permeable disks in the attendance of externally produced magnetic field. Here, we ignore the Hall current effect and body forces, i.e., induced magnetic field due to the presence of external pressure by providing low magnitude of permeable Reynold number. Single-phase simulation was developed for the problem at hand in the presence of different types of nanoparticles. Permeable disks are located at equal distances from the center and moving up and down with distance 2s(t), along with velocity s'(t). Here, the base fluid is water to support our single-phase simulation of the hybrid nanofluids flow. The triadic type of hybrid composite material was introduced here, in which metallic particles of copper are commuted with different metallic-oxide nanomaterials. It is noted that the temperature and concentration of the lower disk are strictly greater than those of the upper disk, as exhibited in Figure 1.

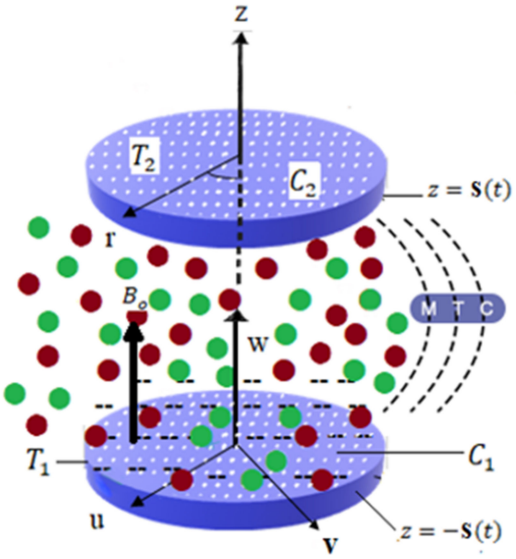

Figure 1. Physical model.

The constitutive expressions can be written as follows [60]:

$$\frac{\partial u}{\partial r}+\frac{u}{r}+\frac{\partial w}{\partial z}=0, \tag{1}$$

$$\frac{\partial u}{\partial t}+u\frac{\partial u}{\partial r}+w\frac{\partial u}{\partial z}-\frac{v^2}{r}=-\frac{1}{\rho_{hnf}}\frac{\partial p}{\partial r}+\upsilon_{hnf}\left(\frac{\partial^2 u}{\partial r^2}+\frac{1}{r}\frac{\partial u}{\partial r}-\frac{u}{r^2}+\frac{\partial^2 u}{\partial z^2}\right)-\frac{\sigma_e B_0^2}{\rho_{hnf}}u, \tag{2}$$

$$\frac{\partial v}{\partial t}+u\frac{\partial v}{\partial r}+w\frac{\partial v}{\partial z}+\frac{uv}{r}=\upsilon_{hnf}\left(\frac{\partial^2 v}{\partial r^2}+\frac{1}{r}\frac{\partial v}{\partial r}-\frac{v}{r^2}+\frac{\partial^2 v}{\partial z^2}\right)-\frac{\sigma_e B_0^2}{\rho_{hnf}}v, \tag{3}$$

$$\frac{\partial w}{\partial t}+u\frac{\partial w}{\partial r}+w\frac{\partial w}{\partial z}=-\frac{1}{\rho_{hnf}}\frac{\partial p}{\partial z}+\upsilon_{hnf}\left(\frac{\partial^2 w}{\partial r^2}+\frac{1}{r}\frac{\partial w}{\partial r}+\frac{\partial^2 w}{\partial z^2}\right) \tag{4}$$

$$\frac{\partial T}{\partial t}+u\frac{\partial T}{\partial r}+w\frac{\partial T}{\partial z}=\alpha_{hnf}\frac{\partial^2 T}{\partial z^2}+\frac{\mu_{hnf}}{(\rho c)_{p_{hnf}}}\left(\frac{\partial u}{\partial z}\right)^2+\frac{\sigma_e B_0^2\, u^2}{(\rho c_p)_{hnf}} \tag{5}$$

$$\frac{\partial C}{\partial t}+u\frac{\partial C}{\partial r}+w\frac{\partial C}{\partial z}=\frac{\partial^2 C}{\partial z^2} \tag{6}$$

$$\upsilon_{hnf}=\frac{\mu_{hnf}}{\rho_{hnf}} \text{ and } \alpha_{hnf}=\frac{k_{hnf}}{(\rho c_p)_{hnf}}, Pr=\frac{(\mu C_p)_{bf}}{k_{bf}} \tag{7}$$

where ρ_s and ρ_f represent the densities of solid particles, particles and fluid; $(c_p)_{hnf}$ shows the heat capacitance of hybrid nanofluids; and k_{hnf} is the thermal conductivity of the hybrid nanofluids.

Uniform mixing of nanoparticles and hosting liquid with negligible slip is presumed in the single-phase approach, which produces thermophysical characteristics that are found by experimental calculation. The accuracy of this approach is predominantly dependent on the accurate prediction of the thermophysical properties of the nanofluids, which are thus presently estimated using the same property correlations utilized in the respective experimental study [51].

Boundary Condition

The associated boundary conditions are as follows:

$$z_1 = -s(t)\ u = 0\ v = -\frac{rA_1 s'(t)}{2s}\ w = -A_1 s'(t)\ T = T_1\ C = C_1$$

and

$$z_1 = s(t)\ u = 0\ v = \frac{rA_1 s'(t)}{2s}\ w = A_1 s'(t)\ T = T_2\ C = C_2 \quad (8)$$

For elimination of the pressure term, the following similarity variables are utilized:

$$\eta = \tfrac{z_1}{s}\ \mathrm{u} = -\tfrac{rv_f}{s^2}F_\eta(\eta,t)\ \mathrm{v} = \tfrac{rv_f}{s^2}G(\eta,t)\ \mathrm{w} = \tfrac{2v_f}{s}F(\eta,t) \qquad \theta = \tfrac{T-T_2}{T_1-T_2}\ ,\ \chi(\eta) = \tfrac{C-C_2}{C_1-C_2},$$

and

$$\frac{v_{hnf}}{v_f}F_{\eta\eta\eta\eta} + \alpha(3F_{\eta\eta} + \eta F_{\eta\eta\eta}) - 2FF_{\eta\eta\eta} - \frac{s^2}{v_f}F_{\eta\eta t} + 2GG_\eta - \frac{\rho_f}{\rho_{hnf}}\mathrm{M}F_{\eta\eta} = 0, \quad (9)$$

$$\frac{v_{hnf}}{v_f}G_{\eta\eta} + \alpha(2G + \eta F_\eta) + 2GF_\eta - \frac{s^2}{v_f}G_t - 2FG_\eta - \frac{\rho_f}{\rho_{hnf}}\mathrm{M}G = 0, \quad (10)$$

$$\theta_{\eta\eta} + \frac{v_f}{\alpha_{hnf}}(\alpha\eta - 2F)\theta_\eta + [(1-(\varphi_1+\varphi_2))^{-2.5}{F_\eta}^2 + M{F_\eta}^2]E_c P_r\frac{\kappa_f}{\kappa_{hnf}} - \frac{k^2}{\alpha_{nf}}\theta_t = 0, \quad (11)$$

$$D\chi'' + v_f\left(\alpha\eta - 2F\right)\chi' - k^2\chi_t = 0, \quad (12)$$

Boundary conditions in dimensionless form are as follows:

$$\eta = -1,\ F = -Re, F_\eta = 0, \theta = 1, \chi = 1,$$

and

$$\eta = 1,\ F = Re, F_\eta = 0, \theta = 0,\ \chi = 0$$

where $\alpha = \frac{ss'(t)}{v_f}$ stands for wall expansion ratio, $\mathrm{Re} = \frac{A_1 ss'(t)}{2v_f}$ stands for permeable Reynold number, $Pr = \frac{(\mu c_p)_f}{k_f}$ stands for the Prandtl number, $Ec = \frac{U^2}{(T_1-T_2)(c_p)_f}$ stands for Eckert number, $P_e = Re * P_r$ is the Peclet number, $\mathrm{Sc} = \frac{v_f}{D}$ stands for Schmidt number, and $\mathrm{M} = \frac{\sigma_e B_0^2 s^2}{\mu_f}$ stands for magnetic parameter referred to [60,61].

Finally, we set F = f Re, G = g Re by following Majdalani et al. [61] when α is a constant.

$f = f$ (η) and $\theta = \theta(\eta)$, which leads to $\theta_t = 0$, $g_{\eta t} = 0$, $f_{\eta\eta t} = 0$, and $\chi_t = 0$. Thus, we have the following equations:

$$\frac{v_{hnf}}{v_f}f_{\eta\eta\eta\eta} + \alpha(3f_{\eta\eta} + \eta f_{\eta\eta\eta}) - 2ff_{\eta\eta\eta} + 2Regg_\eta - \frac{\rho_f}{\rho_{hnf}}Mf_{\eta\eta} = 0 \quad (13)$$

$$\frac{v_{hnf}}{v_f}g_{\eta\eta} + \alpha(2g + \eta g_\eta) + 2Re\left(gf_\eta - fg_\eta\right) - \frac{\rho_f}{\rho_{hnf}}Mg = 0 \quad (14)$$

$$\theta_{\eta\eta} + \frac{v_f}{\alpha_{hnf}}Pr(\alpha\eta - 2Ref)\theta_\eta + [(1-(\varphi_1+\varphi_2))^{-2.5}{f_{\eta\eta}}^2 + M{f_\eta}^2]ReE_c P_e\frac{\kappa_f}{\kappa_{hnf}} = 0 \quad (15)$$

$$\chi'' + Sc(\alpha\eta - 2fRe)\chi' = 0 \quad (16)$$

$$\eta = -1;\ f = -1,\ f_\eta = 0, \theta = 1,\ \chi = 1$$

and

$$\eta = 1;\ f = 1,\ f_\eta = 0, \theta = 0\ \chi = 0. \quad (17)$$

3. Practical and Engineering Interest

3.1. Skin Friction Coefficients

The C_{f1} and C_{f-1} are expressed as follows:

$$\begin{aligned} C_{f-1} &= \frac{\xi_w|_{\eta=-1}}{\rho_{bf}(s'A_1)^2} \\ &= \frac{(1+0.1008((\varphi_1)^{0.69574}\left(dp_1\right)^{0.44708}+(\varphi_2)^{0.69574}(dp_2)^{0.44708}\right)}{Re_r}\sqrt{(f''(-1))^2+(g'(-1))^2} \\ C_{f1} &= \frac{\xi_w|_{\eta=1}}{\rho_{bf}(s'A_1)^2} = \frac{(1+0.1008((\varphi_1)^{0.69574}\left(dp_1\right)^{0.44708}+(\varphi_2)^{0.69574}(dp_2)^{0.44708}\right)}{Re_r}\sqrt{(f''(1))^2+(g'(1))^2} \end{aligned} \tag{18}$$

where ξ_w stand for total shear stress and $Re_r = 4\left(\frac{s}{r}\right)\left(\frac{1}{(Re)^2}\right)$ stands for local the Reynold number.

$$\xi_{zr} = \mu_{hnf}\left(\frac{\partial u}{\partial z}\right)|_{\eta=-1} = \mu_{bf}(1+0.1008((\varphi_1)^{0.69574}\left(dp_1\right)^{0.44708}+(\varphi_2)^{0.69574}(dp_2)^{0.44708}\right)\left(\frac{rv_f}{s^3}\right)f''(-1)$$

$$\xi_{\theta z} = \mu_{hnf}\left(\frac{\partial v}{\partial z}\right)|_{\eta=-1} = \mu_{bf}(1+0.1008((\varphi_1)^{0.69574}\left(dp_1\right)^{0.44708}+(\varphi_2)^{0.69574}(dp_2)^{0.44708}\right)\left(\frac{rv_f}{s^3}\right)g'(-1)$$

3.2. Nusselt Numbers

Nu_{z-1} and Nu_{z1} are given as

$$\begin{aligned} Nu_{z-1} &= \frac{se_z}{\kappa_f(T_1-T_2)}|_{\eta=-1} = -\frac{k_{hnf}}{k_f}\theta'(-1) \\ Nu_{z1} &= \frac{se_z}{\kappa_f(T_1-T_2)}|_{\eta=1} = -\frac{k_{hnf}}{k_f}\theta'(1) \end{aligned} \tag{19}$$

Here, heat flux is denoted as s_z, which is as follows:

$$e_z|_{\eta=-1} = -k_{hnf}\left(\frac{\partial T}{\partial z}\right)|_{\eta=-1} = -\frac{(T_1-T_2)}{s}k_{hnf}\theta'(-1)$$

$$e_z|_{\eta=1} = -k_{hnf}\left(\frac{\partial T}{\partial z}\right)|_{\eta=1} = -\frac{(T_1-T_2)}{s}k_{hnf}\theta'(1)$$

where $Re = \frac{A_1 ss'(t)}{2v_f}$.

3.3. Sherwood Number

Sherwood number is the ratio of convectional mass transfer and diffusion mass transfer. The mass transfer rate (Sherwood number) $Sh|_{\eta=-1}$ and $Sh|_{\eta=1}$ at the lower and upper disk have the following mathematical expression:

$$\begin{aligned} Sh|_{\eta=-1} &= \frac{kq_z}{D_{hnf}(C_1-C_2)}|_{\eta=-1} = -\chi'(-1) \\ Sh|_{\eta=1} &= \frac{kq_z}{D_{hnf}(C_1-C_2)}|_{\eta=1} = -\chi'(1) \end{aligned} \tag{20}$$

where

$$q_z|_{\eta=-1} = -D_{hnf}\left(\frac{\partial C}{\partial z}\right)|_{\eta=-1} = -D_{hnf}\frac{(C_1-C_2)}{k}\chi'(-1)$$

$$q_z|_{\eta=1} = -D_{hnf}\left(\frac{\partial C}{\partial z}\right)|_{\eta=1} = -D_{hnf}\frac{(C_1-C_2)}{k}\chi'(1)$$

where $Re = \frac{A_1 ss'(t)}{2v_f}$.

3.4. Thermophysical Properties

PDE Equations (13)–(16) have appropriate thermophysical properties:

$$\left(\frac{(1+0.1008((\varphi_1)^{0.69574}\left(dp_1\right)^{0.44708}+(\varphi_2)^{0.69574}(dp_2)^{0.44708}\right)}{\left((1-(\varphi_1+\varphi_2))+(\varphi_1)\left(\frac{\rho_{s_1}}{\rho_{bf}}\right)+(\varphi_2)\left(\frac{\rho_{s_2}}{\rho_{bf}}\right)\right)}\right)f''''[\eta]-\alpha(3f''[\eta]+\eta f'''[\eta])-$$
$$2Ref[\eta]f'''[\eta]-\left(\frac{1}{\left((1-\varphi_1-\varphi_2)+\varphi_1\left(\frac{\rho_{s_1}}{\rho_{bf}}\right)+\varphi_2\left(\frac{\rho_{s_2}}{\rho_{bf}}\right)\right)}\right)\mathrm{M}\,f''[\eta]=0 \tag{21}$$

$$\left(\frac{(1+0.1008((\varphi_1)^{0.69574}\left(dp_1\right)^{0.44708}+(\varphi_2)^{0.69574}(dp_2)^{0.44708}\right)}{\left((1-(\varphi_1+\varphi_2))+(\varphi_1)\left(\frac{\rho_{s_1}}{\rho_{bf}}\right)+(\varphi_2)\left(\frac{\rho_{s_2}}{\rho_{bf}}\right)\right)}\right)g''[\eta]+\alpha(2g[\eta]+\eta g'[\eta])+$$
$$2Re(g[\eta]f'[\eta]-f[\eta]g'[\eta])-\left(\frac{1}{\left((1-\varphi_1-\varphi_2)+\varphi_1\left(\frac{\rho_{s_1}}{\rho_{bf}}\right)+\varphi_2\left(\frac{\rho_{s_2}}{\rho_{bf}}\right)\right)}\right)Mg[\eta]=0 \tag{22}$$

$$\theta''[\eta]$$
$$+\Big((1-(\varphi_1+\varphi_2))+(\varphi_1)\left(\frac{\rho_{cps_1}}{\rho_{cpbf}}\right)$$
$$+(\varphi_2)\left(\frac{\rho_{cps_2}}{\rho_{cpbf}}\right)\Big)\left(\frac{k_{s2}+(N-1)k_{mbf}+\varphi_2\left(k_{mbf}-k_{s2}\right)}{k_{s2}+(N-1)k_{mbf}-(N-1)\varphi_2\left(k_{mbf}-k_{s2}\right)}\right)\left(\frac{k_{s1}+(N-1)k_{bf}+\varphi_1\left(k_{bf}-k_{s1}\right)}{k_{s1}+(N-1)k_{bf}-(N-1)\varphi_1\left(k_{bf}-k_{s1}\right)}\right)$$
$$Pr\Big(\alpha\eta-2Ref[\eta])\theta'[\eta]+[(1-(\varphi_1+\varphi_2))^{-2.5}{f_{\eta\eta}}^2+$$
$$M{f_\eta}^2]ReE_cP_e\left(\frac{k_{s2}+(N-1)k_{mbf}+\varphi_2\left(k_{mbf}-k_{s2}\right)}{k_{s2}+(N-1)k_{mbf}-(N-1)\varphi_2\left(k_{mbf}-k_{s2}\right)}\right)\left(\frac{k_{s1}+(N-1)k_{bf}+\varphi_1\left(k_{bf}-k_{s1}\right)}{k_{s1}+(N-1)k_{bf}-(N-1)\varphi_1\left(k_{bf}-k_{s1}\right)}\right)=0 \tag{23}$$

$$\chi''[\eta]+\mathrm{Sc}(\alpha\eta-2\mathrm{Re}f[\eta])\chi'[\eta]=0 \tag{24}$$

$$H_1=\left(\frac{(1+0.1008((\varphi_1)^{0.69574}\left(dp_1\right)^{0.44708}+(\varphi_2)^{0.69574}(dp_2)^{0.44708}\right)}{\left((1-(\varphi_1+\varphi_2))+(\varphi_1)\left(\frac{\rho_{s_1}}{\rho_{bf}}\right)+(\varphi_2)\left(\frac{\rho_{s_2}}{\rho_{bf}}\right)\right)}\right) \tag{25}$$

$$H_2=\left(\frac{1}{\left((1-\varphi_1-\varphi_2)+\varphi_1\left(\frac{\rho_{s_1}}{\rho_{bf}}\right)+\varphi_2\left(\frac{\rho_{s_2}}{\rho_{bf}}\right)\right)}\right) \tag{26}$$

$$H_3=\left((1-(\varphi_1+\varphi_2))+(\varphi_1)\left(\frac{\rho_{cps_1}}{\rho_{cpbf}}\right)+(\varphi_2)\left(\frac{\rho_{cps_2}}{\rho_{cpbf}}\right)\right) \tag{27}$$

$$D_1=\left(\frac{k_{s2}+(N-1)k_{mbf}+\varphi_2\left(k_{mbf}-k_{s2}\right)}{k_{s2}+(N-1)k_{mbf}-(N-1)\varphi_2\left(k_{mbf}-k_{s2}\right)}\right) \tag{28}$$

$$D_2=\left(\frac{k_{s1}+(N-1)k_{bf}+\varphi_1\left(k_{bf}-k_{s1}\right)}{k_{s1}+(N-1)k_{bf}-(N-1)\varphi_1\left(k_{bf}-k_{s1}\right)}\right) \tag{29}$$

$$\omega=D_1D_2. \tag{30}$$

Putting values of (25)–(30) in Equations (21)–(24), the final result is

$$H_1f''''[\eta]-\alpha(3f''[\eta]+\eta f'''[\eta])-2Ref[\eta]f''[\eta]-H_2\,\mathrm{M}\,f''[\eta]=0 \tag{31}$$

$$H_1g''[\eta]+\alpha(2g[\eta]+\eta g'[\eta])+2Re\big(g[\eta]f'[\eta]-f[\eta]g'[\eta]\big)-H_2Mg[\eta]=0 \tag{32}$$

$$\theta''[\eta]+H_3\omega Pr\Big(\alpha\eta-2Ref[\eta])\theta'[\eta]+\omega[(1-(\varphi_1+\varphi_2))^{-2.5}{f_{\eta\eta}}^2+M{f_\eta}^2]ReE_cP_e=0 \tag{33}$$

$$\chi''[\eta]+\mathrm{Sc}(\alpha\eta-2\mathrm{Re}f[\eta])\chi'[\eta]=0 \tag{34}$$

3.5. Solution Procedure

This segment is presented for the discussion of the implemented numerical scheme and steps involved during the simulations. For this purpose, firstly, Equations (13)–(16) with boundary conditions along with effective thermophysical properties are solved numerically by implementing the numerical scheme renowned as RK 4th order in conjunction with the shooting method. To achieve the solution from these procedures, initially, numerical values are choose carefully to accomplish the desired level of accuracy. Owing to low computation cost and memory loss and provision of accurate and consistent results in less time, Runge–Kutta and shooting methods are applied.

4. Result and Discussion

In the present section, results on both the graphical and tabular form against different parameters such as the expansion/contraction ratio parameter (α), permeable Reynold parameter (Re), magnetic parameter (M), Prandtl number (Pr), diameter/size of the nanoparticles (dp_1) and (dp_2), shape factor of the nanoparticles (N), Peclet number (Pe), and Eckert number (Ec), as well as nanoparticle volume fraction (φ) on velocity, temperature and mass distributions, shear stress, and heat and mass transfer rate, are examined thoroughly.

Tables 1 and 2 present the thermophysical properties of (HNFDs) and base fluid with different types of nanoparticles (NPs). Table 3 shows the effect of diameter, volume fraction, and Reynold number on shear stresses by considering three different types of compositions for hybridize NPs, as well as shear stress showing an increasing pattern as compared with tensional stress with an injection factor. Similarly, behavior is observed for the variation in the size of metallic oxides for all types of nanoparticles (Al_2O_3, TiO_2, and Fe_3O_4) compared with copper. Nanoparticles have unique features as compared with bulk material of the same structure. The most common properties of the nanoparticles, for example, can be easily rehabilitated by varying their size and shape. Copper nanomaterials have high thermal conductivity as well as electrical conductivity. The most common shape of copper is round visibility, such as black powder. On the other hand, metal oxide nanoparticles are a very important technological material and have many industrial applications.

Table 1. Thermophysical properties of HNFDs [62–66].

Properties	(HNFDs)
Density (ρ)	$\rho_{hnf} = \varphi_1\rho_{s_1} + \varphi_2\rho_{s\ 2} + (1-\varphi_1-\varphi_2)\,\rho_{bf}$
Viscosity (μ)	$\mu_{hnf} = \mu_{bf}(1 + 0.1008\ ((\varphi_1)^{0.69574}(dp_1)^{0.44708} + (\varphi_2)^{0.69574}(\,dp_2)^{0.44708}))$
Heat Capacity (ρC_P)	$(\rho c_p)_{hnf} = \varphi_1(\rho c_p)_{s_1} + \varphi_2(\rho c_p)_{s_2} + (1-\varphi_1-\varphi_2)\,(\rho c_p)_{bf}$
Thermal Conductivity (K)	$k_{hnf} = \left(\frac{k_{s2}+(N-1)k_{mbf}+\varphi_2(k_{mbf}-k_{s2})}{k_{s2}+(N-1)k_{mbf}-(N-1)\varphi_2(k_{mbf}-k_{s2})}\right)k_{bf}$ where $k_{bf} = \left(\frac{k_{s1}+(N-1)k_{bf}+\varphi_1(k_{bf}-k_{s1})}{k_{s1}+(N-1)k_{bf}-(N-1)\varphi_1(k_{bf}-k_{s1})}\right)k_f$

Table 2. Properties of base fluids and NPs [67].

Base Fluid/NP's	$\rho(\mathbf{kgm^{-3}})$	C_p (J $\mathbf{kg^{-1}k^{-1}}$)	$\kappa\left(\mathbf{wm^{-1}k^{-1}}\right)$
H_2O	997.1	4179	0.613
Cu	8933	385	401
Al_2O_3	3970	765	40
Fe_3O_4	5180	670	9.7
TiO_2	4250	686.2	8.9538

Table 3. Different parameters of the effect in shear stress and tensional stress.

					$Cu\text{-}Al_2O_3/H_2O$		$Cu\text{-}TiO_2/H_2O$		$Cu\text{-}Fe_3O_4/H_2O$	
dp_1	dp_2	φ_1	φ_2	Re	$f''(-1)$	$g'(-1)$	$f''(-1)$	$g'(-1)$	$f''(-1)$	$g'(-1)$
1	1	0.01	0.01	0.2	2.0587	−1.7628	2.0593	−1.7629	2.0615	−1.7633
2					2.0604	−1.7545	2.0611	−1.7547	2.0632	−1.7551
3					2.0616	−1.7484	2.0623	−1.7485	2.0644	−1.7489
4					2.0627	−1.7434	2.0634	−1.7435	2.0654	−1.7439
1	2				2.0604	−1.7546	2.0611	−1.7547	2.0632	−1.7551
	3				2.0616	−1.7484	2.0623	−1.7485	2.0645	−1.7489
	4				2.0627	−1.7434	2.0633	−1.7435	2.0656	−1.7439
	1	0.02			2.0799	−1.7519	2.0806	−1.7521	2.0828	−1.7524
		0.03			2.1009	−1.7429	2.1016	−1.7432	2.1038	−1.7433
		0.04			2.1218	−1.7349	2.1225	−1.7351	2.1247	−1.7353
			0.02		2.0684	−1.7499	2.0697	−1.7502	2.0741	−1.7509
			0.03		2.0777	−1.7392	2.0797	−1.7395	2.0862	−1.7405
			0.04		2.0868	−1.7296	2.0894	−1.7300	2.0981	−1.7313
				0.4	2.2258	−2.1202	2.2271	−2.1215	2.2312	−2.1259
				0.6	2.4441	−2.6358	2.4463	−2.6394	2.4536	−2.6511
				0.8	2.7414	−3.4364	2.7452	−3.4452	2.758	−3.4747

If we increase the nanoparticle level fraction of copper from 1% to 4%, then shear stress is an increasing function; a similar trend is also observed for metallic oxide nanoparticle fraction. The injection phenomenon is very important for biomedical sciences [46]. When increasing the numerical values of injection number in Table 3, both shear and tensional stresses show an increasing pattern. Table 4 calculates the Nusselt number with different shape factors for hybridizing nanofluids ($Cu\text{-}TiO_2/H_2O$, $Cu\text{-}Fe_3O_4/H_2O$, $Cu\text{-}Al_2O_3/H_2O$). If we increase the values of nanoparticles volume fraction, φ_1 and φ_2, then the shape factor of ($Cu\text{-}Al_2O_3/H_2O$) shows better performance than the others. Table 5 demonstrates the effect of the permeable Reynold number Re, expansion ratio α, and Sc on Sherwood number of $Cu\text{-}Al_2O_3/H_2O$. Sherwood number has significant results for the suction case, as compared with injection, when $\alpha > 0$. An opposite trend is observed for contracting and expanding cases when $Re < 0$. If we increase the numerical values of S, then there is a very significant effect on the Sherwood number. Table 6 displays the effect of different parameters on the heat transfer rate at the lower porous disk. Increases in the Pr and Re numbers significantly enhance the heat transfer rate at the lower porous disk, while, on the other hand, N(shape factor) and M (MHD) have a small effect on the heat transfer rate. The Prandtl number Pr, in our problem, the relative importance of the fluid's viscosity and thermal conductivity, appears to raise the actual fluid temperature. Table 7 represents the influence of the magnetic parameter $M > 0$ on the shear stress, tensional stress, and heat transfer rate, and they are all gradually enhanced in the presence of 2% hybrid nanoparticles with the injection case too. In Figure 2, we examine the effect of four types of shape factors on hybrid nanofluid flow associated with a different numerical range of φ_1 and φ_2. All shape factors lie on the x-axis and thermal conductivity varies on the y-axis. A high thermal conductivity value is achieved at 5.7 when the nanoparticle volume fraction is at 1. Thermal conductivity is an increasing function of the shape factor with the nanoparticle volume fraction. We can say that morphology is directly proportional to the thermal conductivity of any nanofluids. By taking equal numerical values of φ_1 and φ_2, in Figure 3, with a viscosity of base fluids and diameter of all nanoparticles along with different numerical values of morphology (spherical, bricks, cylindrical, and platelets), the X-axis denotes the size factor and the y-axis represents the effective viscosity. Furthermore, the effect of viscosity is very high for a size factor of 12.73 when the nanoparticle volume fraction level is 1%. We also observed that platelet-shaped nanocomposites show a better performance on heat and mass transferability as compared with the other shapes of nanoparticles. Figures 4 and 5 show the effect of a magnetic parameter in the tangent velocity profile and the temperature profile influence of fixed value $\alpha = 1, Re = 1, Pr = 6.2, Ec = 0.00068$. By

increasing the numerical values of the magnetic parameter M, the momentum boundary layer thickness decreases from both porous walls in the presence of $\varphi_1 = \varphi_2 = 1\%$. The physically generated Lorentz force by amplification of the magnetic field generates a resistance to flow and decreases the momentum boundary layer thickness, which is why heat is the main source of heat production. The conclusion is suitable for the fact that the magnetic field implemented is a resistance force that plays a crucial role in decelerating and directing fluid flow. Figure 5 shows the increasing behavior of the temperature profile from the center and covers the whole domain. Figure 6 is drawn to show the nature of the Schmidt number concerning the concentration profiles $\chi(\eta)$. The Schmidt number is, theoretically, the conceptual interaction of momentum and mass diffusivity. Owing to the value of the Schmidt number, the diffusivity increases as a function of the decline in fluid concentration. The value of the Schmidt number is inversely proportional to the diffusivity of the Brownian movement. The greater diffusivity of Brownian corresponds to lower concentration profiles of $\chi(\eta)$. With the increase in the value of the Schmidt number, concentration boundary later thickness is an increasing function of Sc in the presence of $\varphi_1 = \varphi_2 = 3\%$. Figure 7 represents the temperature profile with various values of the Peclet number. With the increase in the value of P_e, the flow of heat transfer enhancement is significantly increased from both porous disks in the presence of $\varphi_1 = \varphi_2 = 5\%$. Physically, the product of Reynold number and Prandtl number is equal to Peclet number which tends to reduce flow velocity in downstream directions and the current factors tend to be one-way properties. In the common perception, it is expected that particles made from high thermal conductivity material should impose high thermal conductivity on nanofluids, but this is not necessary; on the other hand, a famous scientist, Lee et al. [52], conducted experiments with AL_2O_3 and CuO as hybrid nanofluids and reported that, though AL_2O_3 material had a higher thermal conductivity than CuO, CuO as a nanofluid possesses higher thermal conductivity. The investigator claimed reason that AL_2O_3 nanoparticles form a larger nanocluster than CuO nanoparticles in the base fluid water. Hence, some other factor may also be involved.

Table 4. The effect of different hybridized nanoparticles on Nusselt number (Nu).

	Cu-TiO_2/H_2O				**Cu-Fe_3O_4/H_2O**				**Cu-Al_2O_3/H_2O**			
$\varphi_1 = \varphi_2$	$\lvert Nu(3)\rvert$	$\lvert Nu(3.7)\rvert$	$\lvert Nu(4.8)\rvert$	$\lvert Nu(5.7)\rvert$	$\lvert Nu(3)\rvert$	$\lvert Nu(3.7)\rvert$	$\lvert Nu(4.8)\rvert$	$\lvert Nu(5.7)\rvert$	$\lvert Nu(3)\rvert$	$\lvert Nu(3.7)\rvert$	$\lvert Nu(4.8)\rvert$	$\lvert Nu(5.7)\rvert$
1%	1.8586	2.4807	3.2553	3.7454	1.8801	2.4908	3.2586	3.7565.	2.1023	2.7721	3.6048	4.1293
2%	4.4101	4.9099	5.4021	5.6378	4.4251	4.9128	5.4092	5.6484	4.6134	5.1103	5.5781	5.7749
3%	5.5102	5.7584	5.9028	5.8985	5.5122	5.7651	5.914	5.909	5.616	5.8326	5.9358	5.8346
4%	5.9063	5.9308	6.2162	6.3539	5.8959	5.9459	6.4308	6.8651	5.9212	5.9652	6.5901	6.6571

Table 5. Different parameter *Re* (Reynold number), α (wall expansion parameter) *Sc* (Schmidt number) effects on Sherwood number.

			Cu-Al_2O_3/H_2O
Re	***α***	***Sc***	$\lvert Sh\rvert_{\eta=-1}\rvert$
−1.5	1	1	0.19442
−1			0.30838
1			1.30681
1.5			1.69612
−1	−2		0.62786
	−1		0.30838
	1		0.23170
	2		0.05776
	−1	2	2.58310
		4	5.6498
		6	8.7222
		8	11.754

Table 6. The effect of different physical nondimensional parameters Re, α (wall expansion), M (magneitc parameter), N (shape factor), Ec (Eckert number), Pr (Prandtl number), Pe (Peclet number) θ (temperature) on heat transfer.

Re	α	*M*	*N*	Ec	Pr	Pe	$\lvert\theta'(-1)\rvert$
0.3	0.1	1	3	0.000068	6.2	6.8	1.3807
0.6							2.9588
0.9							4.6361
1.2							5.5035
0.3	0.2						1.1974
	0.3						1.0301
	0.4						0.8791
	0.1	4					1.3661
		7					1.3539
		11					1.3405
		1	3.7				1.3660
			4.8				1.3438
			5.7				1.3265
			3	0.00078			1.3805
				0.00088			1.3803
				0.00098			1.3801
					5.7		1.2891
					6.7		1.4756
					7.7		1.6741
						2.8	1.3817
						5.8	1.3810
						8.8	1.3803

Table 7. Magnetic-filed effect in $f''(\eta)$, $g'(\eta)$ and $\theta'(\eta)$ at lower wall $= -1$, $Re = 1$, $\varphi_1 = \varphi_2 = 0.02$, $Ec = 0.00068$, $Pr = 6.2$.

	Cu-Al_2O_3/H_2O		
M	$\lvert f'(-1)\rvert$	$\lvert g'(-1)\rvert$	$\lvert\theta'(-1)\rvert$
3	5.5298	3.8675	0.4361
5	5.838	4.2893	1.6694
7	6.1241	4.6544	3.4804
9	6.3914	4.9794	6.0671
11	6.6429	5.2744	8.4787
13	6.8808	5.546	10.7512
15	7.1069	5.7994	12.9101

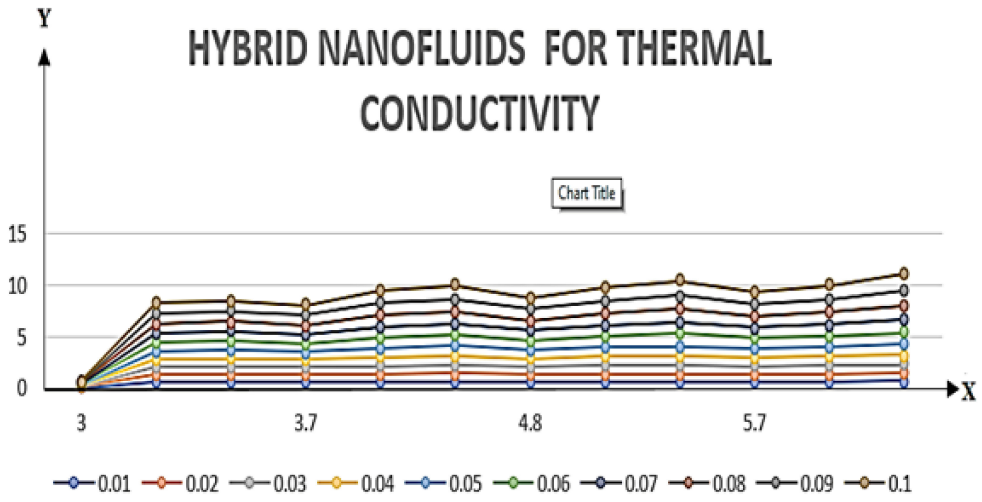

Figure 2. The influence of the scale of hybrid NPs under the thermal conductivity coloring umbrella. Reprinted from [68].

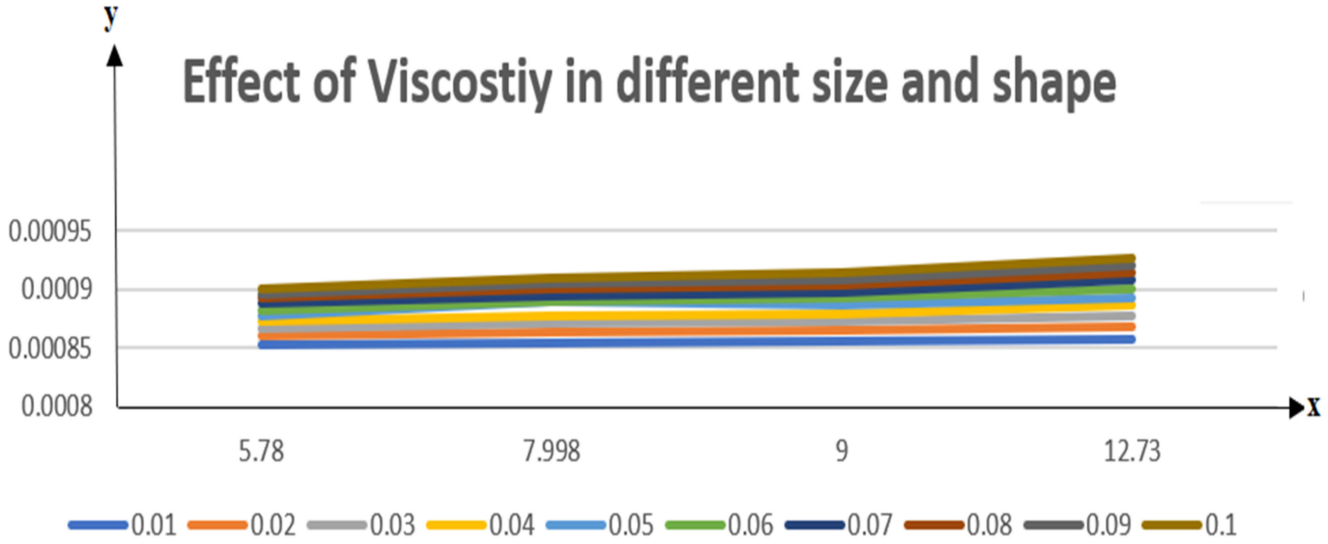

Figure 3. The influence of the scale of hybrid NPs under the viscosity coloring umbrella. Reprinted from [68].

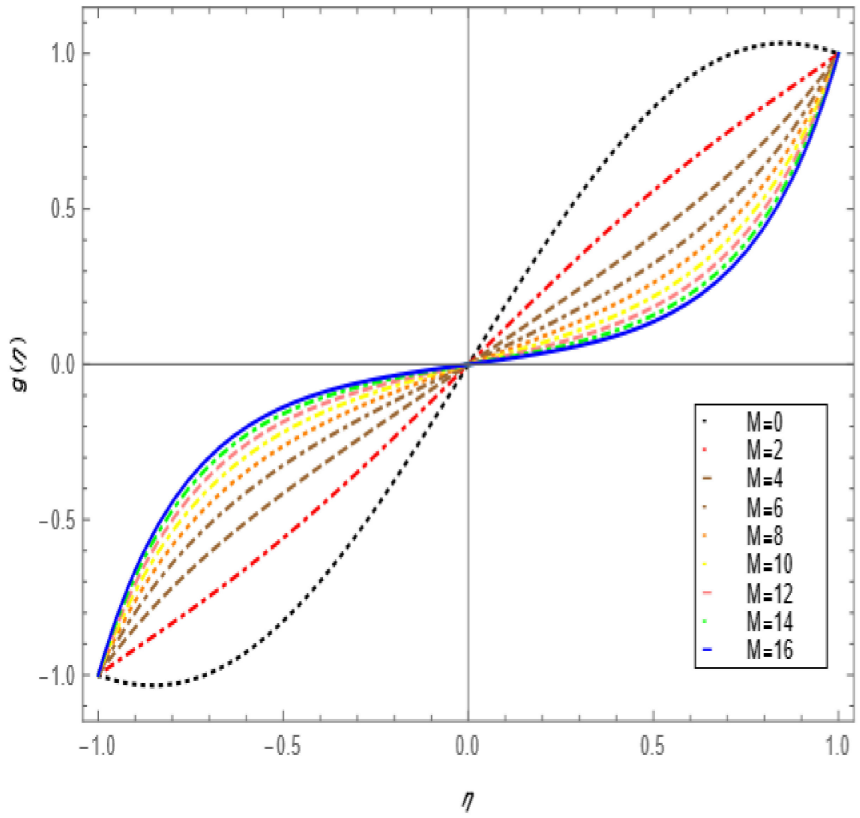

Figure 4. Tangential velocity profile effect for magnetic parameter for $= 1$, $Re = 1$, $\varphi_1 = \varphi_2 = 0.01$, $Ec = 0.00068$, $Pr = 6.2$.

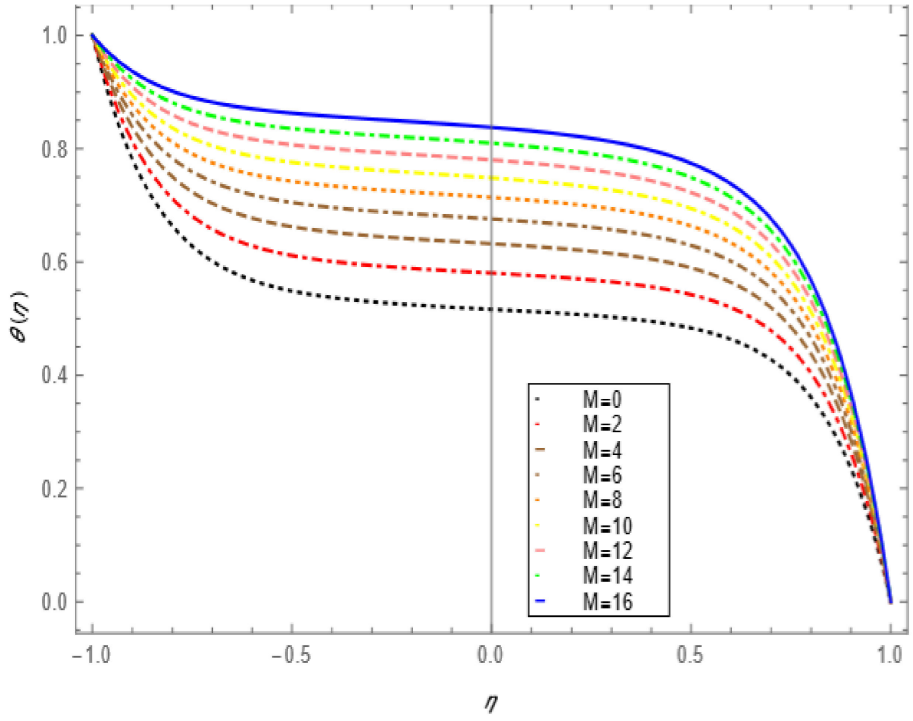

Figure 5. Temperature profile effect for magnetic parameter for $= 1$, $Re = 1$, $\varphi_1 = \varphi_2 = 0.01$, $Ec = 0.00068$, $Pr = 6.2$.

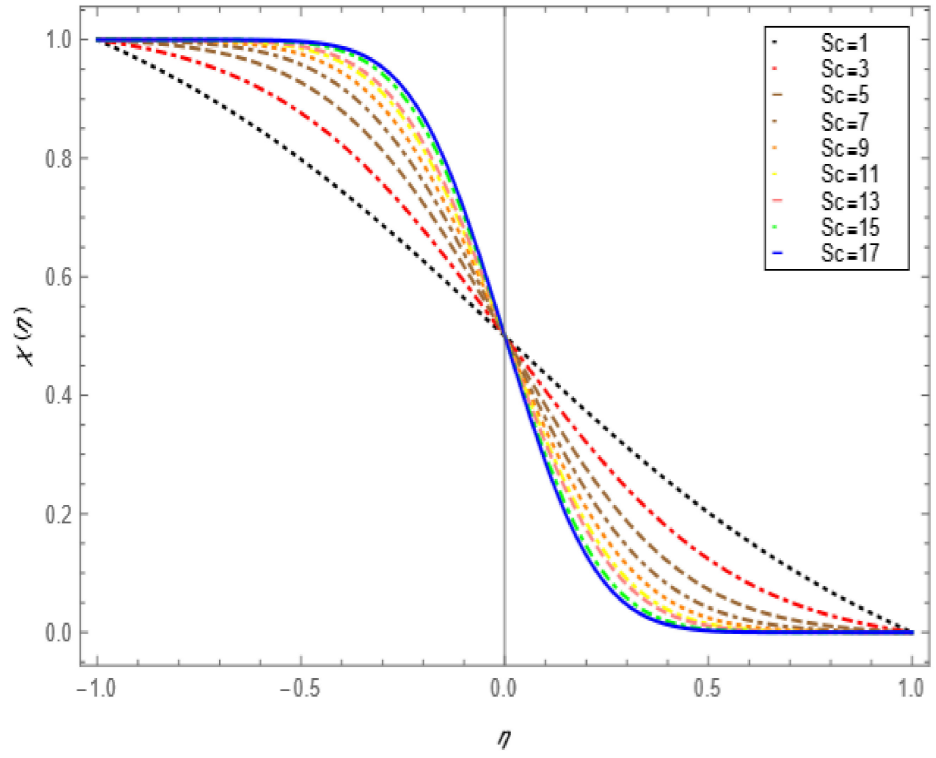

Figure 6. Concentration profile effect for Schmidt number for $= -1, Re = -1$, $\varphi_1 = \varphi_2 = 0.03$, $Ec = 0.00068$, $Pr = 6.2, M = 1$.

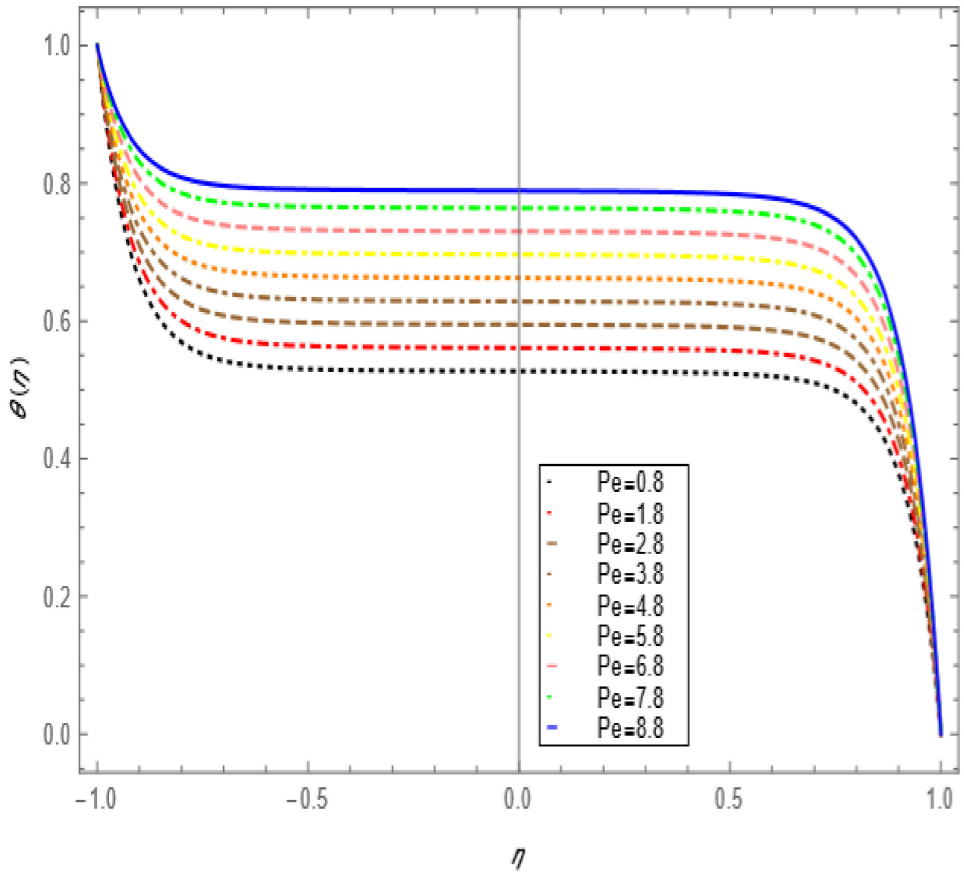

Figure 7. Temperature profile effect size for $= 0.1, Re = 1.5, M = 5, \varphi_1 = \varphi_2 = 0.05, Ec = 0.00068, Pr = 6.2$.

5. Conclusions

We explore the three-dimensional triadic hybrid nanofluid flow behavior with heat and mass transfer aspects in this manuscript, as well as the Newtonian fluid flow through orthogonal porous disks with MHD effects. Metallic and metallic-oxide nanoparticles with morphology effect are considered here. The most important findings are as follows.

Thermal conductivity and viscosity intensity are the highest in HNFD3 with platelet nanoparticles, followed by spherical, brick, and cylindrical nanoparticles, respectively.

By increasing the values magnetic field M, expansion ratio α, and Peclet Pe, there is an improvement in the rate of heat transfer on the porous disk.

- With an increase in the values of volume fraction, the Nusselt number has the largest effect on HNF3 with platelet nanoparticles.
- The momentum boundary layer is gradually increased if we increase the values of permeable Reynold number Re, the diameter of nanoparticles dp_1 and dp_2, and magnetic parameter M.
- If the volume fraction φ_1 and φ_2, the diameter of nanoparticles dp_1 and dp_2, and chemical reaction of Reynold number Re values are greater than zero, then the rate of shear stress and tensional stress is enhanced.
- By raising the Schmidt number Sc and chemical reaction Reynold number Re, the rate of mass transfer on the porous disk is enhanced.

Author Contributions: Conceptualization, Writing-original draft Z.A.Q.; Methodology, Results and discussion S.B.; Results finding, Writing—original draft I.A.S.; Code Validation A.A.; Incorporation of review comments, funding R.J.; Correction of Language, Funding H.S.; Proofreading, Incorporation

of Reviewer Comments, Funding J.A. All authors have read and agreed to the published version of the manuscript.

Funding: The authors R.J., H.S.S. and J.A. would like to thank Palestine Technical university—Kadoorie for funding this work. Scientific research funding 2022.

Institutional Review Board Statement: Not applicable.

Informed Consent Statement: Not applicable.

Data Availability Statement: All data is available in the manuscript.

Conflicts of Interest: The authors declare no conflict of interest.

Nomenclature

B_o	Uniform magnetic field [T]	F_η	Dimensionless radial velocity profile
G_η	Dimensionless tangential velocity profile		
C_f	Total skin friction coefficient	θ_η	Dimensionless temperature profile
C_p	Specific heat at constant pressure	σ	Electrical conductivity $[(m^3A^2)/\mathrm{kg}]$
s	Time depended coefficient	v	Kinematic viscosity $[m^2/\mathrm{s}]$
M	Magnetic parameter	μ	Dynamic viscosity $[P_a.\mathrm{s}]$
P_r	Prandtl number	ρ	Density $[\mathrm{kg}/m^3]$
r z	Cylindrical coordinates system	ρC_P	Volumetric heat capacity [J/(m3 K)]
Re	Reynold number	T	(HN_{fd}) temperature [K]
u, v, w	velocity component along z axis	A_1	Dimensionless parameter coefficient
Nu(HN_{fd})	Nusselt number	$(\rho c_p)_{hnf}$	specific heat capacity for
ρ_{hnf}	Density for (HN_{fd})	ρ_{s1}	Density for first solid NP's
ρ_{s2}	Density for second solid NP's	k_{hnf}	Thermal conductivity for (HN_{fd})
k_{s1}	Thermal conductivity for first solid fraction	k_{s2}	Thermal conductivity for second solid fraction
k_{mbf}	Thermal conductivity for shape base fluid	P	pressure
k_{bf}	Thermal conductivity for base fluid	μ_{eff}	viscosity for effect
μ_{bf}	viscosity base fluid	dp	Dimeter of nanoparticles
dp_1	Dimeter of first nanoparticles	dp_2	dimeter of 2nd nanoparticles
v_{hnf}	Kinematics viscosity for (HN_{fd})	Nu_z	Nusselt number
Sc	Schmidt number	Pe	Pectlet number
Ec	Eckert number	N	Size factor
Subscripts			
(B_{fd})	Base fluid	(NFs)	Nanofluids
(HNFDs)	Hybrid nanofluids		
HNFD1	Cu-TiO_2 /H_2O	HNFD2	Ag-Fe_3O_4/H_2O
HNFD3	Cu-Al_2O_3 /H_2O		
Greek Symbols			
α	Thermal diffusivity $[m^2/\mathrm{s}]$	η	Independent similarity variable
φ	Equivalent nanoparticles volume fraction		
φ_1	Equivalent first nanoparticles volume fraction	φ_2	Equivalent first nanoparticles volume fraction

References

1. Festa, R.A.; Thiele, D.J. Copper: An essential metal in biology. *Curr. Biol.* **2011**, *21*, R877–R883. [CrossRef]
2. Lutsenko, S.; Barnes, N.L.; Bartee, M.Y.; Dmitriev, O.Y. Function and Regulation of Human Copper-Transporting ATPases. *Physiol. Rev.* **2007**, *87*, 1011–1046. [CrossRef]
3. De Bie, P.; Muller, P.; Wijmenga, C.; Klomp, L.W.J. Molecular pathogenesis of Wilson and Menkes disease: Correlation of mutations with molecular defects and disease phenotypes. *J. Med Genet.* **2007**, *44*, 673–688. [CrossRef]
4. Gupta, A.; Lutsenko, S. Human copper transporters: Mechanism, role in human diseases and therapeutic potential. *Future Med. Chem.* **2009**, *1*, 1125–1142. [CrossRef] [PubMed]
5. Majewski, M.; Ognik, K.; Zdunczyk, P.; Juskiewicz, J. Effect of dietary copper nanoparticles versus one copper (II) salt: Analysis of vasoreactivity in a rat model. *Pharmacol. Rep.* **2017**, *69*, 1282–1288. [CrossRef] [PubMed]
6. Tümer, Z.; Møller, L.B. Menkes disease. *Eur. J. Hum. Genet.* **2010**, *18*, 511–518. [CrossRef] [PubMed]
7. Lorincz, M.T. Wilson disease and related copper disorders. *Handb. Clin. Neurol.* **2018**, *147*, 279–292. [CrossRef]

8. Glod, D.; Adamczak, M.; Bednarski, W. Selected aspects of nanotechnology applications in food production. *Żywność Nauka Technol. Jakość* **2014**, *5*, 36–52.
9. Assadi, Z.; Emtiazi, G.; Zarrabi, A. Hyperbranched polyglycerol coated on copper oxide nanoparticles as a novel core-shell nano-carrier hydrophilic drug delivery model. *J. Mol. Liq.* **2018**, *250*, 375–380. [CrossRef]
10. Cholewińska, E.; Juśkiewicz, J.; Ognik, K. Comparison of the effect of dietary copper nanoparticles and one copper (II) salt on the metabolic and immune status in a rat model. *J. Trace Elem. Med. Biol.* **2018**, *48*, 111–117. [CrossRef]
11. Turcu, R.; Darabont, A.L.; Nan, A.; Aldea, N.; Macovei, D.; Bica, D.; Vekas, L.; Pana, O.; Soran, M.L.; Koos, A.A.; et al. New polypyrrole-multiwall carbon nanotubes hybrid materials. *J. Optoelectron. Adv. Mater.* **2006**, *8*, 643–647.
12. Jana, S.; Salehi-Khojin, A.; Zhong, W.-H. Enhancement of fluid thermal conductivity by the addition of single and hybrid nano-additives. *Thermochim. Acta* **2007**, *462*, 45–55. [CrossRef]
13. Devi, S.A.; Devi, S.S.U. Numerical investigation of hydromagnetic hybrid Cu–Al2O3/water nanofluid flow over a permeable stretching sheet with suction. *Int. J. Nonlinear Sci. Numer. Simul.* **2016**, *17*, 249–257. [CrossRef]
14. Devi, S.S.U.; Devi, S.A. Numerical investigation of three-dimensional hybrid Cu–Al2O3/water nanofluid flow over a stretching sheet with effecting Lorentz force subject to Newtonian heating. *Can. J. Phys.* **2016**, *94*, 490–496. [CrossRef]
15. Imran, M.; Farooq, U.; Waqas, H.; Anqi, A.E.; Safaei, M.R. Numerical performance of thermal conductivity in Bioconvection flow of cross nanofluid containing swimming microorganisms over a cylinder with melting phenomenon. *Case Stud. Therm. Eng.* **2021**, *26*, 101181. [CrossRef]
16. Anitha, S.; Safaei, M.R.; Rajeswari, S.; Pichumani, M. Thermal and energy management prospects of γ-AlOOH hybrid nanofluids for the application of sustainable heat exchanger systems. *J. Therm. Anal. Calorim.* **2021**, *27*, 123–142. [CrossRef]
17. Ebrahimi, D.; Yousefzadeh, S.; Akbari, O.A.; Montazerifar, F.; Rozati, S.A.; Nakhjavani, S.; Safaei, M.R. Mixed convection heat transfer of a nanofluid in a closed elbow-shaped cavity (CESC). *J. Therm. Anal. Calorim.* **2021**, *144*, 2295–2316. [CrossRef]
18. Karman, T.V. Über laminare und turbulente reibung. *Z. Angew. Math. Mech.* **1921**, *1*, 1233–1252. [CrossRef]
19. Griffiths, P.T. Flow of a generalized Newtonian fluid due to a rotating disk. *J. Non-Newton. Fluid Mech.* **2015**, *221*, 9–17. [CrossRef]
20. Cochran, W.G. The flow due to a rotating disk. In *Mathematical Proceedings of the Cambridge Philosophical Society*; Cambridge University Press: Cambridge, UK, 1934; Volume 30, pp. 365–375.
21. Stewartson, K. On the flow between two rotating coaxial disks. In *Mathematical Proceedings of the Cambridge Philosophical Society*; Cambridge University Press: Cambridge, UK, 1953; Volume 49, pp. 333–341.
22. Mellor, G.L.; Chapple, P.J.; Stokes, V.K. On the flow between a rotating and a stationary disk. *J. Fluid Mech.* **1968**, *31*, 95–112. [CrossRef]
23. Arora, R.C.; Stokes, V.K. On the heat transfer between two rotating disks. *Int. J. Heat Mass Transf.* **1972**, *15*, 2119–2132. [CrossRef]
24. Kumar, S.K.; Tacher, W.I.; Watson, L.T. Magnetohydrodynamic flow between a solid rotating disk and a porous stationary disk. *Appl. Math. Model.* **1989**, *13*, 494–500. [CrossRef]
25. Waini, I.; Ishak, A.; Pop, I. Agrawal flow of a hybrid nanofluid over a shrinking disk. *Case Stud. Therm. Eng.* **2021**, *25*, 100950. [CrossRef]
26. Turkyilmazoglu, M. Nanofluid flow and heat transfer due to a rotating disk. *Comput. Fluids* **2014**, *94*, 139–146. [CrossRef]
27. Turkyilmazoglu, M. Three dimensional MHD stagnation flow due to a stretchable rotating disk. *Int. J. Heat Mass Transf.* **2012**, *55*, 6959–6965. [CrossRef]
28. Hayat, T.; Qayyum, S.; Imtiaz, M.; Alsaedi, A. Flow between two stretchable rotating disks with Cattaneo-Christov heat flux model. *Results Phys.* **2016**, *7*, 126–133. [CrossRef]
29. Hayat, T.; Nasir, T.; Khan, M.I.; Alsaedi, A. Non-Darcy flow of water-based single (SWCNTs) and multiple (MWCNTs) walls carbon nanotubes with multiple slipconditions due to rotating disk. *Results Phys.* **2018**, *9*, 390–399. [CrossRef]
30. Ghadikolaei, S.S.; Hosseinzadeh, K.; Ganji, D.D. Investigation on three dimensional squeezing flow of mixture base fluid (ethylene glycol-water) suspended by hybrid nanoparticle (Fe3O4-Ag) dependent on shape factor. *J. Mol. Liq.* **2018**, *262*, 376–388. [CrossRef]
31. Chamkha, A.J.; Dogonchi, A.S.; Ganji, D.D. Magneto-hydrodynamic flow and heat transfer of a hybrid nanofluid in a rotating system among two surfaces in the presence of thermal radiation and Joule heating. *AIP Adv.* **2019**, *9*, 025103. [CrossRef]
32. Gholinia, M.; Armin, M.; Ranjbar, A.; Ganji, D. Numerical thermal study on CNTs/ $C_2H_6O_2$– H_2O hybrid base nanofluid upon a porous stretching cylinder under impact of magnetic source. *Case Stud. Therm. Eng.* **2019**, *14*, 100490. [CrossRef]
33. Ghachem, K.; Aich, W.; Kolsi, L. Computational analysis of hybrid nanofluid enhanced heat transfer in cross flow micro heat exchanger with rectangular wavy channels. *Case Stud. Therm. Eng.* **2020**, *24*, 100822. [CrossRef]
34. Abedalh, S.A.; Shaalan, A.Z.H.; Yassien, N.S. Mixed convective of hybrid nanofluids flow in a backward-facing step. *Case Stud. Therm. Eng.* **2021**, *25*, 100868. [CrossRef]
35. Xu, H. Modelling unsteady mixed convection of a nanofluid suspended with multiple kinds of nanoparticles between two rotating disks by generalized hybrid model. *Int. Commun. Heat Mass Transf.* **2019**, *108*, 104275. [CrossRef]
36. Acharya, N.; Bag, R.; Kundu, P.K. Influence of Hall current on radiative nanofluid flow over a spinning disk: A hybrid approach. *Phys. E Low-Dimens. Syst. Nanostruct.* **2019**, *111*, 103–112. [CrossRef]
37. Dinarvand, S.; Rostami, M.N. An innovative mass-based model of aqueous zinc oxide–gold hybrid nanofluids for von Karman's swirling flow. *J. Therm. Anal. Calorim.* **2019**, *138*, 845–855. [CrossRef]
38. Khan, M.; Ali, W.; Ahmed, J. A hybrid approach to study the influence of Hall current in radiative nanofluid flow over a rotating disk. *Appl. Nanosci.* **2020**, *10*, 5167–5177. [CrossRef]

39. Izadi, M.; Mohebbi, R.; Karimi, D.; Sheremet, M.A. Numerical simulation of natural convection heat transfer of nanofluid with Cu, MWCNT, and Al2O3 nanoparticles in a cavity with different aspect ratios. *Chem. Eng. Process. Process Intensif.* **2018**, *125*, 56–66. [CrossRef]
40. Arani, A.A.A.; Akbari, O.A.; Safaei, M.R.; Marzban, A.; Alrashed, A.A.; Ahmadi, G.R.; Nguyen, T.K. Heat transfer improvement of water/single-wall carbon nanotubes (SWCNT) nanofluid in a novel design of a truncated double-layered microchannel heat sink. *Int. J. Heat Mass Transf.* **2017**, *113*, 780–795. [CrossRef]
41. Safaei, M.R.; Ahmadi, G.; Goodarzi, M.S.; Kamyar, A.; Kazi, S.N. Boundary Layer Flow and Heat Transfer of FMWCNT/Water Nanofluids over a Flat Plate. *Fluids* **2016**, *1*, 31. [CrossRef]
42. Goshayeshi, H.R.; Safaei, M.R.; Goodarzi, M.; Dahari, M. Particle size and type effects on heat transfer enhancement of Ferro-nanofluids in a pulsating heat pipe. *Powder Technol.* **2016**, *301*, 1218–1226. [CrossRef]
43. Akbari, O.A.; Safaei, M.R.; Goodarzi, M.; Akbar, N.S.; Zarringhalam, M.; Shabani, G.A.S.; Dahari, M. A modified two-phase mixture model of nanofluid flow and heat transfer in a 3-D curved microtube. *Adv. Powder Technol.* **2016**, *27*, 2175–2185. [CrossRef]
44. Safaei, M.R.; Shadloo, M.S.; Goodarzi, M.; Hadjadj, A.; Goshayeshi, H.R.; Afrand, M.; Kazi, S.N. A survey on experimental and numerical studies of convection heat transfer of nanofluids inside closed conduits. *Adv. Mech. Eng.* **2016**, *8*. [CrossRef]
45. Vajravelu, K.; Prasad, K.V.; Ng, C.-O.; Vaidya, H. MHD squeeze flow and heat transfer of a nanofluid between parallel disks with variable fluid properties and transpiration. *Int. J. Mech. Mater. Eng.* **2017**, *12*, 9. [CrossRef]
46. Das, K.; Jana, S.; Acharya, N. Slip effects on squeezing flow of nanofluid between two parallel disks. *Int. J. Appl. Mech. Eng.* **2016**, *21*, 5–20. [CrossRef]
47. Mohyud-Din, S.T.; Khan, S.I.; Bin-Mohsin, B. Velocity and temperature slip effects on squeezing flow of nanofluid between parallel disks in the presence of mixed convection. *Neural Comput. Appl.* **2017**, *28*, 169–182. [CrossRef]
48. Qayyum, S.; Imtiaz, M.; Alsaedi, A.; Hayat, T. Analysis of radiation in a suspension of nanoparticles and gyrotactic microorganism for rotating disk of variable thickness. *Chin. J. Phys.* **2018**, *56*, 2404–2423. [CrossRef]
49. Aziz, A.; Alsaedi, A.; Muhammad, T.; Hayat, T. Numerical study for heat generation/absorption in flow of nanofluid by a rotating disk. *Results Phys.* **2018**, *8*, 785–792. [CrossRef]
50. Reddy, P.S.; Sreedevi, P.; Chamkha, A.J. MHD boundary layer flow, heat and mass transfer analysis over a rotating disk through porous medium saturated by Cu-water and Ag-water nanofluid with chemical reaction. *Powder Technol.* **2017**, *307*, 46–55. [CrossRef]
51. Muhammad, S.; Ali, G.; Shah, Z.; Islam, S.; Hussain, S.A. The Rotating Flow of Magneto Hydrodynamic Carbon Nanotubes over a Stretching Sheet with the Impact of Non-Linear Thermal Radiation and Heat Generation/Absorption. *Appl. Sci.* **2018**, *8*, 482. [CrossRef]
52. Uddin, I.; Akhtar, R.; Khan, M.A.R.; Zhiyu, Z.; Islam, S.; Shoaib, M.; Raja, M.A.Z. Numerical treatment for fluidic system of activation energy with non-linear mixed convective and radiative flow of magneto nanomaterials with Navier's velocity slip. *AIP Adv.* **2019**, *9*, 055210. [CrossRef]
53. Khan, M.I.; Hayat, T.; Alsaedi, A. A modified homogeneous-heterogeneous reactions for MHD stagnation flow with viscous dissipation and Joule heating. *Int. J. Heat Mass Transf.* **2017**, *113*, 310–317. [CrossRef]
54. Khan, N.; Sajid, M.; Mahmood, T. Heat transfer analysis for magnetohydrodynamics axisymmetric flow between stretching disks in the presence of viscous dissipation and Joule heating. *AIP Adv.* **2015**, *5*, 057115. [CrossRef]
55. Krishna, M.V.; Ahamad, N.A.; Chamkha, A.J. Hall and ion slip impacts on unsteady MHD convective rotating flow of heat generating/absorbing second grade fluid. *Alex. Eng. J.* **2020**, *60*, 845–858. [CrossRef]
56. Krishna, M.V.; Chamkha, A.J. Hall and ion slip effects on MHD rotating boundary layer flow of nanofluid past an infinite vertical plate embedded in a porous medium. *Results Phys.* **2019**, *15*, 102652. [CrossRef]
57. Toghraie, D.; Mashayekhi, R.; Arasteh, H.; Sheykhi, S.; Niknejadi, M.; Chamkha, A.J. Two-phase investigation of water-Al2O3 nanofluid in a micro concentric annulus under non-uniform heat flux boundary conditions. *Int. J. Numer. Methods Heat Fluid Flow* **2019**, *30*, 1795–1814. [CrossRef]
58. Krishna, M.V.; Ahamad, N.A.; Chamkha, A.J. Hall and ion slip effects on unsteady MHD free convective rotating flow through a saturated porous medium over an exponential accelerated plate. *Alex. Eng. J.* **2020**, *59*, 565–577. [CrossRef]
59. Krishna, M.V.; Chamkha, A.J. Hall and ion slip effects on MHD rotating flow of elastico-viscous fluid through porous medium. *Int. Commun. Heat Mass Transf.* **2020**, *113*, 104494. [CrossRef]
60. Ali, K.; Akbar, M.Z.; Iqbal, M.F.; Ashraf, M. Numerical simulation of heat and mass transfer in unsteady nanofluid between two orthogonally moving porous coaxial disks. *AIP Adv.* **2014**, *4*, 107113. [CrossRef]
61. Majdalani, J.; Zhou, C.; Dawson, C.A. Two-dimensional viscous flow between slowly expanding or contracting walls with weak permeability. *J. Biomech.* **2002**, *35*, 1399–1403. [CrossRef]
62. Chamkha, A.J.; Selimefendigil, F. Forced Convection of Pulsating Nanofluid Flow over a Backward Facing Step with Various Particle Shapes. *Energies* **2018**, *11*, 3068. [CrossRef]
63. Ghadikolaei, S.; Hosseinzadeh, K.; Hatami, M.; Ganji, D. MHD boundary layer analysis for micropolar dusty fluid containing Hybrid nanoparticles (Cu-Al_2O_3) over a porous medium. *J. Mol. Liq.* **2018**, *268*, 813–823. [CrossRef]
64. Rostami, M.N.; Dinarvand, S.; Pop, I. Dual solutions for mixed convective stagnation-point flow of an aqueous silica–alumina hybrid nanofluid. *Chin. J. Phys.* **2018**, *56*, 2465–2478. [CrossRef]

65. Sundar, S.; Sharma, K.V.; Singh, M.K.; Sousa, A.C.M. Hybrid nanofluids preparation, thermal properties, heat transfer and friction factor—A review. *Renew. Sustain. Energy Rev.* **2017**, *68*, 185–198. [CrossRef]
66. Selimefendigil, F.; Öztop, H.F.; Chamkha, A.J. Mixed Convection of Pulsating Ferrofluid Flow Over a Backward-Facing Step. *IJST-T Mech. Eng.* **2021**, *43*, 593–612. [CrossRef]
67. Sheikholeslami, M.; Ganji, D.D. Nanofluid flow and heat transfer between parallel plates considering Brownian motion using DTM. *Comput. Methods Appl. Mech. Eng.* **2014**, *283*, 651–663. [CrossRef]
68. Abdelmalek, Z.; Akbar Qureshi, M.Z.; Bilal, S.; Raza, Q.; Sherif, E.S.M. A case study on morphological aspects of distinct magnetized 3D hybrid nanoparticles on fluid flow between two orthogonal rotating disks: An application of thermal energy systems. *Case Stud. Therm. Eng.* **2021**, *23*, 100744. [CrossRef]